

Kinetic effects of trapped energetic particles on stability of external kink modes with a resistive wall

G. Z. Hao, Y. Q. Liu, A. K. Wang, and X. M. Qiu

Citation: *Phys. Plasmas* **19**, 032507 (2012); doi: 10.1063/1.3692185

View online: <http://dx.doi.org/10.1063/1.3692185>

View Table of Contents: <http://pop.aip.org/resource/1/PHPAEN/v19/i3>

Published by the [American Institute of Physics](#).

Related Articles

Tendency of spherically imploding plasma liners formed by merging plasma jets to evolve toward spherical symmetry

Phys. Plasmas **19**, 052702 (2012)

Filamentation instability of quantum magnetized plasma in the presence of an external periodic magnetic field

Phys. Plasmas **19**, 042112 (2012)

Nonlinear saturation amplitudes in classical Rayleigh-Taylor instability at arbitrary Atwood numbers

Phys. Plasmas **19**, 042705 (2012)

The EPED pedestal model and edge localized mode-suppressed regimes: Studies of quiescent H-mode and development of a model for edge localized mode suppression via resonant magnetic perturbations

Phys. Plasmas **19**, 056115 (2012)

Electric field structure inside the secondary island in the reconnection diffusion region

Phys. Plasmas **19**, 042902 (2012)

Additional information on Phys. Plasmas

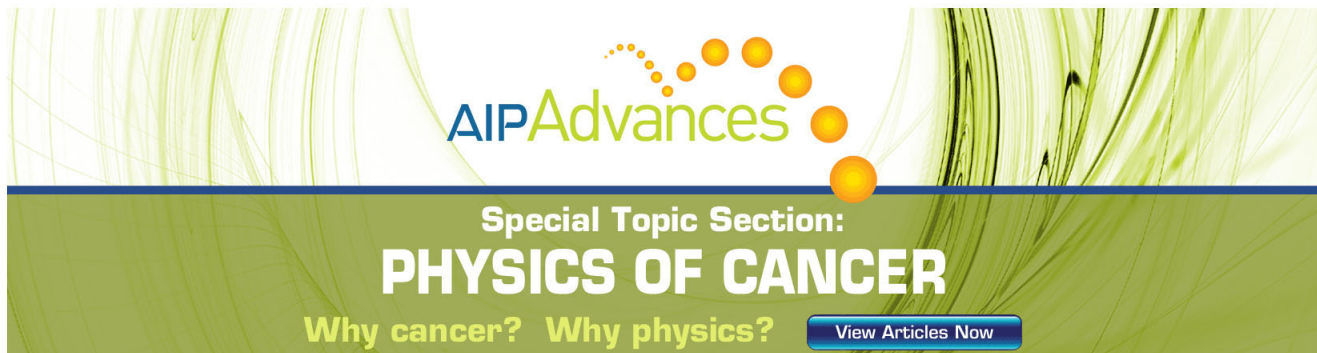
Journal Homepage: <http://pop.aip.org/>

Journal Information: http://pop.aip.org/about/about_the_journal

Top downloads: http://pop.aip.org/features/most_downloaded

Information for Authors: <http://pop.aip.org/authors>

ADVERTISEMENT

The advertisement features a green and white abstract background of curved lines. At the top, the 'AIP Advances' logo is displayed in green and yellow. Below it, the text 'Special Topic Section: PHYSICS OF CANCER' is written in white on a dark green background. At the bottom, the phrase 'Why cancer? Why physics?' is written in yellow, and a blue button with the text 'View Articles Now' is positioned to the right.

AIP Advances

Special Topic Section:
PHYSICS OF CANCER

Why cancer? Why physics? [View Articles Now](#)

Kinetic effects of trapped energetic particles on stability of external kink modes with a resistive wall

G. Z. Hao,^{1,a)} Y. Q. Liu,² A. K. Wang,¹ and X. M. Qiu¹¹Southwestern Institute of Physics, P. O. Box 432, Chengdu 610041, China²Euratom/CCFE Fusion Association, Culham Science Centre, Abingdon, Oxon OX14 3DB, United Kingdom

(Received 2 December 2011; accepted 10 February 2012; published online 22 March 2012)

Kinetic effects of trapped energetic particles (EPs) on stability of the external kink mode with a resistive wall are investigated in detail, on the basis of the theory model developed in a previous paper [G. Z. Hao, A. K. Wang, Y. Q. Liu, and X. M. Qiu, *Phys. Rev. Lett.* **107**, 015001 (2011)]. The results indicate that, when the perpendicular beta β^* of the trapped EPs exceeds a critical value β_c^* , a bursting fishbone-like mode (FLM) instability, with external kink eigenstructure, can be triggered, which rapidly grows with increasing β^* ($> \beta_c^*$), and eventually becomes a dominant instability. Detailed physical analyses are carried out, comparing radial profiles of the EPs kinetic energy for both the FLM and the conventional resistive wall mode (RWM). On the other hand, a mode conversion between the FLM and RWM can directly occur. This work also presents a systematic investigation of effects of various physical parameters on the FLM instability. An interesting new finding is the existence of multiple critical points in β^* , for the FLM triggering. The number of critical points depends sensitively on the trapped EPs pitch angle. In addition, it is found that there can be a critical value of the pitch angle, beyond which the critical β_c^* , for triggering the FLM, jumps from a large value to a small one. The FLM instability, with the $m/n = 3/1$ mode structure, can also be triggered by the trapped EPs. © 2012 American Institute of Physics. [<http://dx.doi.org/10.1063/1.3692185>]

I. INTRODUCTION

Future advanced tokamak devices (such as ITER) need to operate in high- β regions, where β is the ratio of the plasma pressure to the magnetic pressure. However, the achievable β_N (normalized β) is often limited by global magnetohydrodynamic (MHD) instabilities, such as the external kink mode, which can be stabilized by an ideal conducting wall placed close enough to the plasma surface. In practice, the wall has finite resistivity, and hence converting the fast-growing ideal kink mode into a slowly growing mode, the so-called resistive wall mode (RWM). The RWM is unstable when $\beta_N^{no-wall} < \beta_N < \beta_N^{ideal}$, where $\beta_N^{no-wall}$ and β_N^{ideal} denote the beta limits without and with an ideal wall, respectively.

The stabilization of the RWM is an essential issue for the tokamak configuration aiming at long-duration steady discharges over the no-wall beta limit. Theory models have shown that when the plasma toroidal rotation speed exceeds a critical value, the RWM can be completely suppressed by the continuum damping from the resonance interaction between the mode and stable waves inside the plasma, such as the Alfvén wave and the sound wave.^{1–10} In addition, the plasma resistivity and viscosity may also lead to the mode stabilization.^{11,12} In order to explain the experimental observations of a very low critical toroidal rotation speed for the RWM suppression,^{13,14} the drift kinetic models have been proposed for the RWM instability, which show that the resonance interaction between the mode and particle motions can contribute a significant suppression to the RWM.^{15–19} In a slowly rotating plasma, the dissipation from the mode resonance with the

precession drift of the trapped particles provides a dominant stabilization effect. In the fast rotation regime, the kinetic interaction between the mode and the bounce motion of trapped particles, or the transit motion of passing particles, becomes significant.²⁰ Recent observations in DIII-D tokamak have shown that the resonant interaction between the RWM and the thermal particles may be responsible for the improved plasma stability at very low plasma rotation.²¹

The kinetic effect of energetic particles (EPs) on the RWM instability has also been studied in both experiment and theory. It has been shown that trapped EPs can stabilize the RWM and can also trigger a new bursting fishbone-like instability (FLM) at the same time.^{15,22–27} It should be mentioned that various names for the bursting mode have been proposed in literatures, such as “EWM” in JT-60U (Ref. 27) and “off-axis fishbone” in DIII-D,²⁵ respectively. Here, this three letter acronym FLM is introduced mainly for a convenient description of the mode’s nature, not for labeling a “new” mode. Kinetic effects of trapped EPs on external kink modes, in the presence of a resistive wall, have not been fully investigated so far.²⁸ In the present paper, on the basis of a theory model developed in our previous paper,¹⁵ we offer a more detailed understanding of the interaction between trapped EPs and the RWM and FLM instabilities.

The remainder of the paper is organized as follows. Section II describes the kinetic model for the RWM and FLM, where the kinetic effect from trapped EPs is taken into account. In Sec. III, a physical analysis and a parametric investigation of the trapped EPs effects are carried out for the $m/n=2/1$ modes. Section IV presents calculations for the $m/n = 3/1$ modes. Summary and discussions are given in Sec. V.

^{a)}Electronic mail: hao gz@swip.ac.cn.

II. KINETIC MODEL FOR THE RWM AND FLM

The linearized MHD equations, including the perturbed kinetic pressure tensor ($\delta\bar{\mathbf{P}}_h$) due to energetic particles (EPs), are written as

$$-\omega^2 \rho \xi = (\mathbf{J}_0 \times \delta\mathbf{B}_1 + \delta\mathbf{J} \times \mathbf{B}_0) - \nabla \delta P - \nabla \cdot \delta\bar{\mathbf{P}}_h, \quad (1)$$

$$\delta\mathbf{B} = \nabla \times (\xi \times \mathbf{B}_0), \quad (2)$$

$$\delta\mathbf{J} = \frac{1}{\mu_0} \nabla \times \delta\mathbf{B}, \quad (3)$$

$$\delta P = -\xi \cdot \nabla P_0 - \Gamma P_0 \nabla \cdot \xi, \quad (4)$$

$$\begin{aligned} \delta\bar{\mathbf{P}}_h = & -\xi_{\perp} \cdot \nabla [P_{\perp,h} \mathbf{I} + (P_{\parallel,h} - P_{\perp,h}) \mathbf{b}\mathbf{b}] + \delta P_{\perp,h} \mathbf{I} \\ & + (\delta P_{\parallel,h} - \delta P_{\perp,h}) \mathbf{b}\mathbf{b}, \end{aligned} \quad (5)$$

where $\omega = \omega_r + i\gamma$, ρ , μ_0 , and Γ are the mode eigenvalue, the plasma density, the permeability of free space, and the ratio of specific heats, respectively. The variables ξ , $\delta\mathbf{J}$, $\delta\mathbf{B}$, and δP denote the displacement, the perturbed current, the perturbed magnetic field, and the perturbed pressure of the core plasma (thermal species), respectively. The equilibrium current, field, and pressure are labeled by \mathbf{J}_0 , \mathbf{B}_0 , and P_0 , respectively. Moreover, \mathbf{I} is the unit tensor and $\mathbf{b} = \mathbf{B}/B$. ξ_{\perp} is the perpendicular component of the plasma displacement. $P_{\perp,h} = \int m_h \frac{v_{\perp}^2}{2} F_h d^3v$ and $P_{\parallel,h} = \int m_h v_{\parallel}^2 F_h d^3v$ are the perpendicular and parallel (to the equilibrium magnetic field) components of the EPs pressure, while $\delta P_{\perp,h} = \int m_h \frac{v_{\perp}^2}{2} \delta F_h d^3v$ and $\delta P_{\parallel,h} = \int m_h v_{\parallel}^2 \delta F_h d^3v$ denote the perpendicular and parallel components of the EPs perturbed pressure, respectively.^{29–31} m_h is the mass of EPs, v_{\parallel} and v_{\perp} are the parallel and perpendicular velocities of the trapped EPs, respectively. F_h and δF_h are the equilibrium and perturbation of the distribution function of EPs, respectively. The calculation of δF_h is carried out following the procedures as that given in Refs. 29–31.

The total perturbed potential energy, including all of the contributions from the core plasma (δW_P), the EPs (δW_{K0}) and the perturbed magnetic field in the vacuum region (δW_V), can be written as

$$\delta W = \delta W_P + \delta W_{K0} + \delta W_V, \quad (6)$$

$$\begin{aligned} \delta W_P = & \frac{1}{2} \int \left[\frac{|\delta\mathbf{B}|^2}{\mu_0} - \mathbf{J}_0 \cdot (\delta\mathbf{B} \times \xi) + \Gamma P_0 (\nabla \cdot \xi) \right. \\ & \left. + (\xi \cdot \nabla P_0) \nabla \cdot \xi \right] d^3r, \end{aligned} \quad (7)$$

$$\delta W_{K0} = \frac{1}{2} \int [\xi^* \cdot (\nabla \cdot \delta\mathbf{P}_h)] d^3r, \quad (8)$$

$$\delta W_V = \int \frac{|\delta\mathbf{B}|^2}{2\mu_0} d^3r, \quad (9)$$

where $\int \dots d^3r$ denotes the integration over the volume space. It is well known that the stability of the RWM is determined by the following dispersion relation in the absence of the kinetic effect³²

$$D(\omega) \equiv -i\omega\tau_w^* + \frac{\delta W_P + \delta W_V^{\infty}}{\delta W_P + \delta W_V^b} = 0, \quad (10)$$

where δW_V^{∞} and δW_V^b represent the energies due to the perturbed magnetic field in vacuum region (between the plasma surface and the wall position) with an ideal wall placed at infinity and b , respectively. When the effect of the EPs is taken into account, the perturbed potential energy of the core plasma in Eq.(10) (i.e., δW_P) is replaced by $\delta W_P + \delta W_{K0}$.¹⁹ Thus, the RWM dispersion relation, including the kinetic effect of EPs, is obtained as^{3,15,17,18,22}

$$D(\omega) \equiv -i\omega\tau_w^* + \frac{\delta W_f^{\infty} + \delta W_{K0}}{\delta W_f^b + \delta W_{K0}} = 0, \quad (11)$$

where τ_w^* characterizes the typical wall eddy current decay time of a resistive wall. For a circular cylinder $\tau_w^* = \mu_0 \sigma b d (1 - a^{2m}/b^{2m}) / (2m)$, with a , b , d , σ , and m being the plasma minor radius, the wall minor radius, the wall thickness, the wall conductivity, and the poloidal mode number, respectively. $\delta W_f^{\infty} \equiv \delta W_P + \delta W_V^{\infty}$ and $\delta W_f^b \equiv \delta W_P + \delta W_V^b$ represent the perturbed fluid potential energies without and with an ideal wall, respectively. δW_{K0} denotes the perturbed drift kinetic potential energy due to trapped EPs, which consists of a kinetic component δW_k and a fluid component $\delta W_{MHD,h}$. The formula for δW_k and $\delta W_{MHD,h}$ can be found in Ref. 15. Here, δW_k is generally a complex number, while $\delta W_{MHD,h}$ is a real number. In addition, we neglect the inertial term in our dispersion relation, compared to Eq. (1) of Ref. 17. This is because the inertial term is normally negligible for the RWM stability (the mode complex frequency is very small), unless the mode is close to the ideal-wall marginal point.

The mode-particle resonance operator entering into δW_{K0} is³⁰

$$\mathbb{R} = \frac{1}{\omega_d - \omega}, \quad (12)$$

where $\omega_d = K_2 E q / (K_b r \omega_c R)$ is the bounce-averaged precession frequency of the trapped EPs. Here, the value of ω_d depends on both the energy and the radial location of the EPs. ω_c and E are cyclotron frequency and the energy of trapped EPs. q is the safety factor. K_2 and K_b are defined as $2\sqrt{2}/(\epsilon\alpha B_0)(2E - K)/\pi$ and $2\sqrt{2}/(\epsilon\alpha B_0)K/\pi$, respectively. Here, we have introduced K and E to denote the complete elliptic integrals of the first and second kinds, respectively, with the argument $k_t = (1/\alpha B_0 = 0.99 + \epsilon - 1)/(2\epsilon)$, with $\alpha B_0 = 0.99$ and $\epsilon = r/R$ being the pitch angle of trapped EPs and the ratio of the plasma radial variable to the major radius, respectively. The constraint $0 \leq k_t \leq 1$ for the argument of elliptic integrals yields $\hat{r} > \hat{r}_{\min} [= |(1 - 1/\alpha B_0 = 0.99)|R/a]$. This also implies that, with the single pitch angle model for the EPs distribution, $\alpha B_0 = 0.99$ is a special point, in the sense that \hat{r}_{\min} reaches zero only at this special pitch angle. Equation (12) implies that the integration of \mathbb{R} over the velocity space and the volume space will result in the imaginary part [i.e., $\text{Im}(\delta W_{K0})$] of δW_{K0} when $\omega_d - \omega = 0$, due to the Landau resonance.

The real and imaginary parts of Eq. (11) are, respectively, written as

$$\gamma\tau_w^* = \frac{(\delta W_f^b - \delta W_f^\infty)[\delta W_f^b + \text{Re}(\delta W_{K0})]}{\{[\delta W_f^b + \text{Re}(\delta W_{K0})]^2 + \text{Im}(\delta W_{K0})^2\}} - 1, \quad (13)$$

and

$$\omega_r\tau_w^* = \frac{(\delta W_f^b - \delta W_f^\infty)\text{Im}(\delta W_{K0})}{\{[\delta W_f^b + \text{Re}(\delta W_{K0})]^2 + \text{Im}(\delta W_{K0})^2\}}. \quad (14)$$

Without the EPs contribution, Eq. (13) recovers the form given in Ref. 32. Equation (13) implies that the imaginary part of the EPs kinetic contribution [i.e., $\text{Im}(\delta W_{K0})$], which comes from the resonance interaction between the mode rotation with the precession motion of the trapped EPs, always provides stable effects on the instability. However, the real part $\text{Re}(\delta W_{K0})$, induced by the non-resonant effect of the EPs, can provide either stabilization or destabilization effects which is determined by the balance of the perturbed energies in Eq. (13). Furthermore, when $|\text{Im}(\delta W_{K0})| \ll |\delta W_f^b + \text{Re}(\delta W_{K0})|$, the effect of $\text{Re}(\delta W_{K0})$ on γ becomes significant. Figure 1 plots the stability contour in the $\text{Im}(\delta W_{K0})$ versus $\text{Re}(\delta W_{K0})$ plane according to Eq. (13).³³ Inside the shaped region, the RWM is unstable ($\gamma\tau_w^* > 0$). Otherwise, the RWM is stable. The curves labeled by different values of $\gamma\tau_w^*$ denote the contours of constant normalized growth rate. In regions I and II, increasing $|\text{Im}(\delta W_{K0})|$ always results in a decrease of $\gamma\tau_w^*$. As $\text{Im}(\delta W_{K0})$ approaches zero, the growth rate $\gamma\tau_w^*$ significantly depends on $\text{Re}(\delta W_{K0})$. Moreover, the inertia-less model, Eq. (11), also gives a singular point denoted by the circle in the figure, at which $\text{Re}(\delta W_{K0}) = -\delta W_f^b$ and $\text{Im}(\delta W_{K0}) = 0$. Near this singular point, even a very small change of either $\text{Im}(\delta W_{K0})$ or $\text{Re}(\delta W_{K0})$ can lead to a significant change of $\gamma\tau_w^*$. This singularity is removed by adding the inertia term (to the RWM dispersion relation (11)), which will become important near the ideal wall marginal point. In regions III and IV, where $\text{Re}(\delta W_{K0}) < -\delta W_f^b$, the mode is fully stabilized independent of the value of $\text{Im}(\delta W_{K0})$. Finally, we mention that the effect of the plasma viscosity, or the resonance of the mode with

stable waves in plasmas, can give a similar contribution to the RWM kinetic dispersion relation, as the role of δW_{K0} .³

For the classical fishbone instability with internal kink mode structure, the instability growth rate is mainly determined by the plasma fluid perturbed potential energy and the real part of the EPs contribution $\text{Re}(\delta W_{K0})$, which is not directly related to the imaginary part of the EPs drift kinetic energy, as described in Ref. 30. However, in our theory model, Eq. (13) indicates that the growth rate of the mode depends on the plasma fluid perturbed potential energy and on both the real and imaginary parts of δW_{K0} . In addition, Eq. (14) shows that the real frequency of the mode is induced by $\text{Im}(\delta W_{K0})$, and its magnitude depends on both $\text{Im}(\delta W_{K0})$ and $\text{Re}(\delta W_{K0})$, as well as on the perturbed fluid potential energy of the core plasma. However, the real frequency of a classical fishbone mode is determined only by the value of $\text{Im}(\delta W_{K0})$. The above discussions indicate one of the main differences between the dispersion relation used for the FLM and the classical fishbone dispersion relation presented in Ref. 30. Another difference is in the mode eigenfunction, used in the calculation of the perturbed energies.

For simplicity, the external kink mode eigenfunction for a cylindrical equilibrium¹⁷ is used to calculate the perturbed energies. The perpendicular component of mode displacement is taken as $\xi_\perp = amr^{m-1}(\mathbf{e}_r + i\mathbf{e}_\theta)e^{i(m\theta - n\phi)}/F_0$ with n being the toroidal mode number, $F_0 = (m - nq)a/(Rq)$ and $\hat{r} = r/a$. Here, we consider the case of $m = 2$ and $n = 1$. Based on the above assumptions, we obtain the formula of the EPs kinetic contribution to the RWM dispersion relation

$$\begin{aligned} \delta W_{K0} &= 2\pi c_\beta \int_{r_{\min}}^a \hat{r}^{2(m-1)} r dr d\alpha dE E^{5/2} \\ &\times \left\{ \frac{(\omega - \omega_0)K_2^2}{(\omega_d + \omega_0 - \omega)K_b} \frac{\partial}{\partial E} \left(\frac{f}{E^{1/2}} \right) \right. \\ &\left. - \left[\frac{\omega - \omega_0}{\omega_d(\omega_d + \omega_0 - \omega)} \frac{K_2^2}{r\omega_c K_b} - \frac{K_2^2(q-1)}{K_b r\omega_d \omega_c} \right] \frac{\partial}{\partial r} \left(\frac{f}{E^{1/2}} \right) \right\}, \end{aligned} \quad (15)$$

where $c_\beta = \pi N_p \mu_0 m_h / (RB_0 a^2)$ and the energy is normalized to $\pi B^2 a^4 m^2 / 2R\mu_0 F_0^2$. We have used ω_0 to denote the plasma

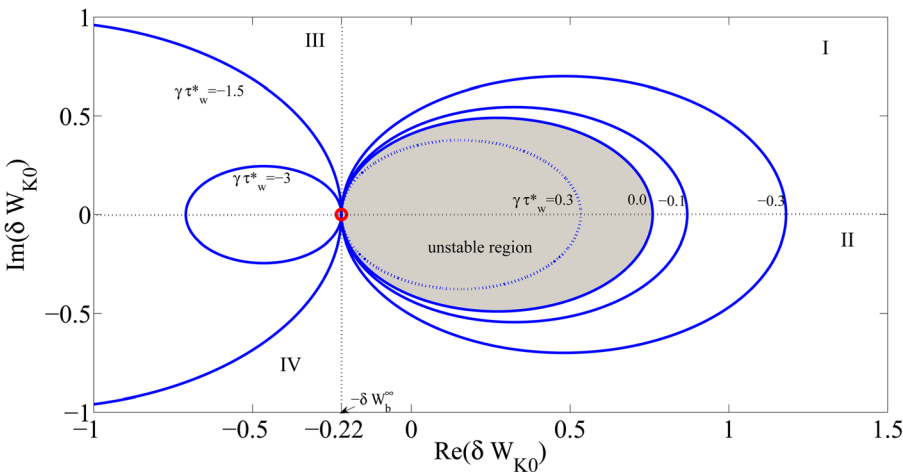


FIG. 1. (Color online) Contour plots of the stability in the plane of $\text{Im}(\delta W_{K0})$ versus $\text{Re}(\delta W_{K0})$, where we choose $\delta W_f^\infty = -0.76$ and $\delta W_f^b = 0.22$ based on the parameters given at the beginning of Sec. III.

rotation frequency (the Doppler shift frequency), which is actually the toroidal component of the $\mathbf{E} \times \mathbf{B}$ flow with \mathbf{E} being the total electric field. $f = 2^{5/2} R \sqrt{EF} / N_p$ is the normalized form of the EPs distribution function, with N_p being the total number of the EPs and F being the EPs distribution function. For the case of the neutral beam heating, the normalized form of a slowing-down distribution function is assumed $f = n_0 E^{-1} \delta(\alpha B_0 - \alpha_0 B_0)$, where $n_0 = 2^{5/2} R n_t / N_p$, with n_t being a constant denoting the flat radial density of EPs. It is worthy to point out that the EPs kinetic energy δW_{K0} , as well as all the resonance analysis presented later on in this paper, is carried out using the self-consistently calculated mode eigenvalue.

Following a straightforward derivation, the kinetic integral can be obtained as

$$\delta W_{K0} = \int_{\hat{r}_{\min}}^1 W(r) d\hat{r} + M, \quad (16)$$

$$W(r) = \beta_n \frac{8\pi}{Aa} \left(1 - \frac{\alpha_0 B_0}{2}\right)^2 R a^{2m-2} \Omega_{pf} \hat{r}^{2(m-1)} \hat{r}^{-1/2} \times \left[\frac{\hat{A} - \hat{B}}{\Omega_{d,e}} \ln(1 - \Omega_{d,e}/\Omega_{pf}) - \frac{\hat{B}}{\Omega_{pf} - \Omega_{d,e}} \right], \quad (17)$$

where $A = \int_{\hat{r}_{\min}}^1 \hat{r}^{1/2} K d\hat{r}$, $\Omega_{d,e} \equiv \omega_{d,e}/\omega_{ds} = E_m K_2 q / (\omega_{ds} K_b r \omega_c R)$, $\Omega_{pf} \equiv \omega_{pf}/\omega_{ds} = i\gamma\tau_w^* / (\tau_w^* \omega_{ds}) + \Omega_r - \Omega_0$, with $\omega_{pf} (\equiv \omega_r + i\gamma - \omega_0)$ being the mode complex frequency in the plasma frame. We have introduced $\gamma\tau_w^*$, $\Omega_r = \omega_r/\omega_{ds}$ and $\Omega_0 = \omega_0/\omega_{ds}$ to denote the normalized mode growth rate, the mode real frequency, and the plasma rotation frequency, respectively. We have used $\omega_{ds} = K_2(a) E_m q / [K_b(a) a \omega_c R]$ to label the bounce-average precession drift frequency of the trapped EPs at the plasma edge with $m_n E_m (\equiv E_b)$ being the birth energy of the beam-driven EPs. The expressions of M and the coefficients \hat{A} and \hat{B} are the same as those given in Ref. 15. Due to the fact that the value of M is much smaller than the first term in the right hand side of Eq. (16), the M term is neglected in further calculations. The choice of different normalizations for the mode growth rate and the mode real frequency is motivated by the convenience of physical interpretation of the results. Whilst the wall time τ_w^* is the convenient choice for measuring the RWM instability, the normalization of Ω_r and Ω_0 , by the EPs precession frequency (at birth energy), better reflects the resonant conditions in our context. In addition, the normalized forms of the fluid potential energies δW_f^∞ and δW_f^b are the same as those given in Ref. 15.

In the case of $q = 1$ and $m = 1$, the coefficients \hat{A} and \hat{B} recover those given in Ref. 34. Figure 2 shows the coefficients \hat{A} , \hat{B} , and $\hat{A} - \hat{B}$ as functions of the normalized minor radius \hat{r} . When \hat{r} approaches unity, \hat{A} and \hat{B} rapidly approach constants. Furthermore, at relatively large \hat{r} , the value of $\hat{A} - \hat{B}$ is much larger than that of \hat{B} , implying that the $\hat{A} - \hat{B}$ (together with other multipliers) term provides the dominant contribution to $W(r)$ in this situation.

We point out that our drift kinetic energy (δW_{K0}) calculations implicitly assume the toroidicity condition (the large aspect ratio expansion), which gives us trapped particles.

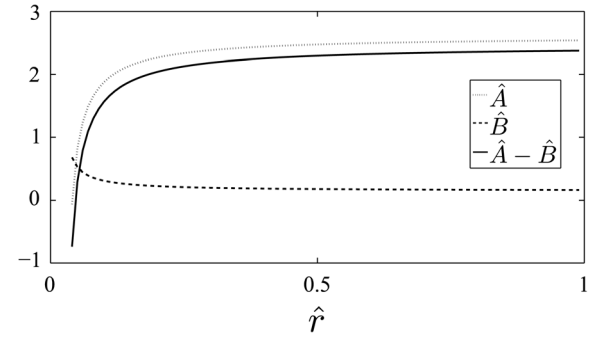


FIG. 2. The coefficients \hat{A} , \hat{B} , and $\hat{A} - \hat{B}$ as functions of the normalized radial variable, for the EPs pitch angle parameter $\alpha_0 B_0 = 0.99$.

However, the fluid potential energy (δW_f^∞ and δW_f^b) calculations are based on a cylindrical geometry. Hence, strictly speaking, our calculation for the RWM instability using Eq. (11) is consistent only at an infinite aspect ratio limit. Nevertheless, the main goal of this work is to provide a qualitative estimate of the linear interaction between trapped EPs and external kink modes. The precise computations, including realistic tokamak effects, such as the plasma toroidicity, the plasma shaping, and the magnetic shear, can only be carried out using numerical codes such as MARS-K, which includes also the kinetic effects of EPs.²⁴ Adding toroidal (and plasma shaping) effect will certainly change the value of the fluid energy. Instead of resorting to analytic formulas for the fluid potential energy in a toroidal plasma, we numerically performed a sensitivity study of our results on the values of the fluid potential energy and found that the toroidal modification on the fluid energy did not change our qualitative conclusions – it only changed the threshold value β_c^* and the corresponding initial real frequency of the mode. The effect of the plasma shaping is more difficult to analyze without numerical tools, and it is not considered in the present work. We point out, though, that the plasma shaping effects (elongation and triangularity) can reduce the trapped EPs precession drift frequency, and hence significantly decrease the EPs β^* threshold for the “standard” fishbone mode.³⁵

III. EFFECTS OF EPS ON THE $m/n=2/1$ MODES

We solve numerically the dispersion relation (11), choosing the following parameters $m = 2$, $n = 1$, $a = 1$ m, $R = 3$ m, $B_0 = 2.3$ T, the EPs birth energy $E_b = 85$ KeV, $q = 1.42$, $\beta = 0.055$, $b = 1.2a$, $\sigma = 10^6 \Omega^{-1} \text{m}^{-1}$, $d = 0.01a$, and the density $n_0 = 10^{20} \text{m}^{-3}$. These operating conditions are chosen, mainly to have a fluid unstable RWM regime in the absence of kinetic effects. In particular, the choice of the harmonic numbers and the q value yields an unstable fluid RWM with $\delta W_f^\infty = -0.76 < 0$ and $\delta W_f^b = 0.22 > 0$. Here, we also assume a flat q -profile to simplify calculations. We point out that the flat q -profile is consistent with our choice of the expression for the magnetic precession frequency, which neglects the terms associated with the magnetic shear. The choice of the wall parameters gives a typical RWM growth rate. The other parameters correspond to a

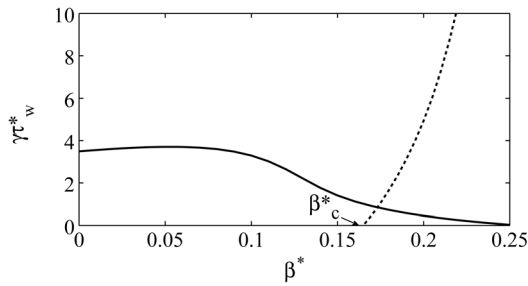


FIG. 3. The growth rate of the RWM (solid curve) and the FLM (dashed curve) as functions of the trapped EPs beta $\beta^* \equiv \beta_h/\beta$ (the fraction of EPs beta to the total plasma beta) for the EPs pitch angle $\alpha_0 B_0 = 0.99$ and the plasma rotation frequency $\Omega_0 = -0.63$.

conventional tokamak plasma, with the neutral-beam-injection induced energetic particles.

A. Stability and physics analysis for a typical case

Figure 3 plots the normalized mode growth rate versus the normalized EPs beta $\beta^* \equiv \beta_h/\beta$ (the fraction of EPs beta to the total plasma beta). When β^* is less than a critical value $\beta_c^* = 0.165$, only one branch of instability (the unstable RWM with the damping effect of the trapped EPs) exists. However, when $\beta^* > \beta_c^*$, there are two unstable branches: one branch (solid curve) is completely suppressed when $\beta^* > 0.25$, with the corresponding real mode frequency (in the wall frame) about 0.156. This is the conventional RWM branch. Stabilization of this branch is achieved solely by the mode resonance with EPs in our model, not by other damping mechanisms such as the mode resonance with thermal particles, or with the Alfvén or sound wave continua. The other branch (dashed curve) is a bursting mode (i.e., FLM), with initial real frequency (in the wall frame) $\Omega_{r,c} = 1.23$ (see Fig. 4). The mode growth rate $\gamma\tau_w^*$ is roughly a linear function of $\beta^* (> \beta_c^*)$. Since all energies in Eq. (11) are calculated based on the external kink mode eigenfunction, the FLM possesses a global eigenstructure. At $\beta^* = 0.2$, the FLM's real frequency in the wall frame is $\omega_r = 1.7 \times 10^4$ rad/s⁻¹ or $f_r = 2.7$ kHz, as shown by Fig. 4, and the corresponding mode growth rate is $\gamma = 2.5 \times 10^3$ s⁻¹. These values are qualitatively comparable with the experimental results of $f_r^{\text{exp}} \approx 3.0$ kHz and $\gamma^{\text{exp}} \approx 1.0 \times 10^3$ s⁻¹.²⁷ The initial real frequency of the FLM instability in the plasma frame is $\Omega_{pf,c} = \Omega_{r,c} - \Omega_0 = 1.86$, where the plasma rotation fre-

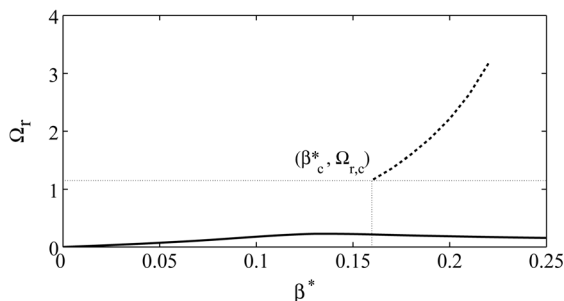


FIG. 4. The real frequency of the RWM (solid curve) and the FLM (dashed curve) versus the trapped EPs beta β^* for the parameters $\alpha_0 B_0 = 0.99$, and $\Omega_0 = -0.63$. The critical point for FLM is labeled by $(\beta_c^*, \Omega_{r,c})$. Here, $\Omega_{r,c}$ denotes the FLM initial real frequency in the wall frame.

quency is chosen as $\Omega_0 = -0.63$. Here, the negative sign of Ω_0 implies that the direction of the plasma rotation is opposite to that of the precession motion of trapped EPs. In this stability analysis, the EPs loss induced by MHD activities is not considered. The FLM's growth rate hence always increases and can approach very large values with increasing the EPs beta. In reality, the long time nonlinear interaction between EPs and the mode will result in the saturation and periodic changes of the FLM growth rate, as observed in experiments.^{23,25}

Shown in Fig. 4 are the frequencies of the FLM and RWM as functions of β^* . For the RWM, the real frequency initially increases with β^* , reaching a maximum value of 0.23 at $\beta^* = 0.14$, followed by a reduction as increasing β^* . This is a typical characteristic of RWM: the mode possesses small real frequencies with respect to the wall. For the FLM, the real frequency of the mode increases with increasing β^* .

Given in Fig. 5 are the imaginary and real parts of δW_{K0} , as function of β^* , for both the FLM and the RWM. The δW_{K0} is calculated using the self-consistently calculated mode eigenvalue while neglecting the small term M in Eq. (16). A discussion about the relation between δW_{K0} and the eigenvalue of the RWM has been presented in Ref. 22. As for the FLM, it is shown that $\text{Im}(\delta W_{K0})$ decreases with increasing β^* . It is well-known that the mode growth rate increases with decreasing $\text{Im}(\delta W_{K0})$ while fixing $\text{Re}(\delta W_{K0})$. In our case, $\text{Re}(\delta W_{K0})$ hardly changes while varying β^* , and its magnitude is comparable to the value of δW_f^b . Hence, as expected, the growth rate of the FLM increases with increasing β^* , as shown by the dashed curve in Fig. 3. In addition, Fig. 5 reveals that the amplitude of $\text{Re}(\delta W_{K0})$ in the FLM case is larger than that in RWM case at the same value of β^* . At the critical point for triggering FLM, both of $[\delta W_f^b + \text{Re}(\delta W_{K0})]$ and $\text{Im}(\delta W_{K0})$ are very small and in the same order of 10^{-2} . The location of the marginal point for triggering FLM in the stability diagram (Fig. 1) is indeed near the singular point. In this situation, both the real and imaginary parts of δW_{K0} can significantly affect the complex frequency of the FLM.

In order to gain insight into the behavior of the FLM instability, the radial profiles of the imaginary part $\text{Im}[W(r)]$ and the real part $\text{Re}[W(r)]$ of the drift kinetic energy, for various values of β^* , are presented in Fig. 6. It shows that when the value of β^* ($=0.166$) approaches to the critical value

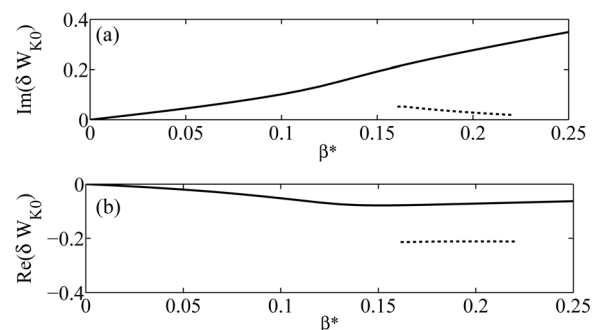


FIG. 5. The (a) imaginary and (b) real parts of δW_{K0} as functions of β^* for the RWM (solid curves) and for the FLM (dashed curves). The other parameters are given as $\alpha_0 B_0 = 0.99$ and $\Omega_0 = -0.63$.

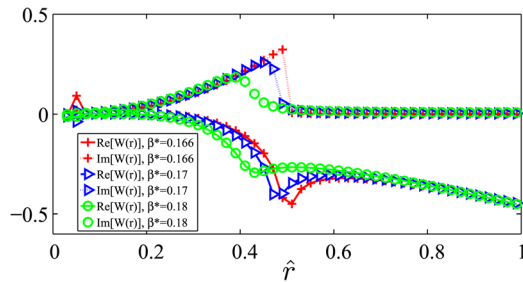


FIG. 6. (Color online) The radial distributions of the imaginary and the real parts of $W(r)$ for different choices of the β^* values. The other parameters are given as $\alpha_0 B_0 = 0.99$ and $\Omega_0 = -0.63$. At $\beta^* = 0.166, 0.17$, and 0.18 , the FLM eigenvalues (normalized to ω_{ds}) are $(1.27 + 0.004i)$, $(1.36 + 0.03i)$, and $(1.60 + 0.11i)$, respectively.

$\beta_c^* (= 0.165)$ for triggering FLM, the value of $\text{Im}[W(r)]$ sharply reduces at the position $\hat{r} = 0.5$ and almost vanishes for large $\hat{r} (> 0.5)$. Since at the special position $\hat{r} = 0.5$, the value of coefficient $\hat{A} - \hat{B}$ is significantly larger than that of \hat{B} as shown in Fig. 2; the term associated with the resonance condition $\ln(1 - \Omega_{d,e}/\Omega_{pf})$, in the definition of $W(r)$ expressed by Eq. (17), is predominant. At the FLM critical point, where the FLM growth rate is zero, the operator $(1 - \Omega_{d,e}/\Omega_{pf,c})$ is a real number, where $\Omega_{pf,c} = 1.86$ denotes the FLM initial real frequency in the plasma frame. Since the factor $\Omega_{d,e}$ is a function of \hat{r} , both cases of $\Omega_{d,e}/\Omega_{pf,c} > 1$ and $\Omega_{d,e}/\Omega_{pf,c} < 1$ are possible depending on the minor radius as shown in Fig. 7. When $\Omega_{d,e}/\Omega_{pf,c} > 1$, the resonance condition $\ln(1 - \Omega_{d,e}/\Omega_{pf,c})$ yields an imaginary part. On the other hand, if $\Omega_{d,e}/\Omega_{pf,c} < 1$, the operator $\ln(1 - \Omega_{d,e}/\Omega_{pf,c})$ only gives a real number. The transition from $\Omega_{d,e}/\Omega_{pf,c} > 1$ to $\Omega_{d,e}/\Omega_{pf,c} < 1$ can result in a sudden drop in $\text{Im}[W(r)]$, which provides a significant influence on the mode growth rate. A comparison between dotted-curves with different symbols in Fig. 6 suggests that the magnitude of $\text{Im}(\delta W_{K0})$ (the radial integral of $\text{Im}[W(r)]$) should increase with decreasing β^* , which is confirmed by the dashed-curve in Fig. 5(a).

At $\beta^* = 0.166$, the magnitude of $\text{Re}[W(r)]$ peaks at the special position $\hat{r} = 0.5$, due to the fact that the value of $1 - \Omega_{d,e}/\Omega_{pf}$ is almost equal to zero at this position (see Fig. 7). We notice that the imaginary part is mostly distributed in the middle of the plasma column, while the real part is more global and tends to increase (by amplitude) with the minor radius. Furthermore, it is expected that the integration of $\text{Re}[W(r)]$, over the minor radius, is less sensitive to the value

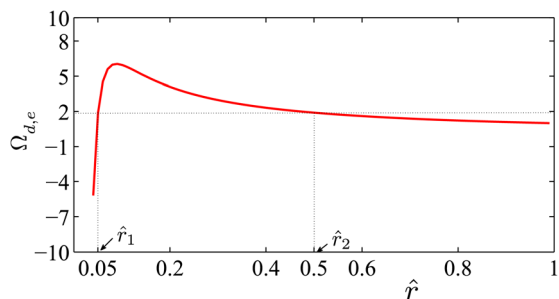


FIG. 7. (Color online) The normalized precession drift frequency of trapped EPs, $\Omega_{d,e}$, versus the minor radius, \hat{r}_1 and \hat{r}_2 , denote the resonant positions at which the precession frequency of the trapped EPs with birth energy is equal to the real frequency of the FLM mode (at $\beta^* = 0.166$).

of β^* , as shown by the dashed curve in Fig. 5(b). The physics reason for the above special radial profiles of $W(r)$ will be discussed in detail later on.

We also notice that both $\text{Im}[W(r)]$ and $\text{Re}[W(r)]$ peak at the position $\hat{r} = 0.05$ at $\beta^* = 0.166$. This is caused by the resonance operator $1/(\Omega_{pf} - \Omega_{d,e})$ in $W(r)$. At this small minor radius, the resonant operator $1/(\Omega_{pf} - \Omega_{d,e})$ is dominant over the factor $\ln(1 - \Omega_{d,e}/\Omega_{pf})$, due to the fact that the value of \hat{B} is much larger than that of $\hat{A} - \hat{B}$ at this minor radius, as shown in Fig. 2. Because of the cancellation of the peaks with opposite signs in the integration over the minor radius, the singularity of $\text{Re}[W(r)]$ at $\hat{r} = 0.05$ does not give much contribution to the value of $\text{Re}[\delta W_{K0}]$.

Given in Fig. 7 is the radial profile of the normalized drift precession frequency of trapped EPs with birth energy. In the region near \hat{r}_{\min} , the sign of precession frequency sharply changes from negative to positive along the minor radius. Figure 7 also shows the special positions $\hat{r}_1 = 0.05$ and $\hat{r}_2 = 0.5$, where the EPs precession frequency $\Omega_{d,e}$ is equal to the real frequency of the FLM $\Omega_{pf,r} (= 1.9)$ of the case of $\beta^* = 0.166$. At these two radial positions (\hat{r}_1, \hat{r}_2), the resonance condition $(1 - \Omega_{d,e}/\Omega_{pf,r} = 0)$ is satisfied. In the region between $\hat{r}_1 = 0.05$ and $\hat{r}_2 = 0.5$, the real frequency of the FLM can resonate with the precession frequency of trapped EPs with a certain kinetic energy (smaller than the birth energy). However, outside this region, there are no EPs that can satisfy the resonance condition $1 - \Omega_{d,e}/\Omega_{pf,r} = 0$ (see Fig. 11).

In order to gain detailed understanding of the kinetic influence of trapped EPs on the RWM instability and to compare the difference between the FLM and RWM cases, the radial profiles of $W(r)$ for the RWM case, for the different values of EPs β^* , are displayed in Fig. 8. The radial profile of $W(r)$ in the RWM case is rather different from that in the FLM case. When the value of EPs beta approaches the critical value $\beta_{c,rwm}^* (= 0.25)$ for a complete suppression of the RWM, as shown in Fig. 3, there is no special radial position, at which $W(r)$ experiences sharp radial variation. At $\beta^* = 0.1, 0.15$, and 0.24 , the RWM eigenvalues (normalized to ω_{ds}) are $(0.17 + 0.22i)$, $(0.22 + 0.09i)$, and $(0.16 + 0.0064i)$, respectively. Figure 8 shows that $\text{Im}[W(r)]$ increases along the minor radius for a fixed EPs beta. Moreover, $\text{Im}[W(r)]$ also increases with increasing β^* , for a fixed minor radius (especially at the plasma edge). The relation between the magnitude of $\text{Im}[W(r)]$ and β^* suggests an

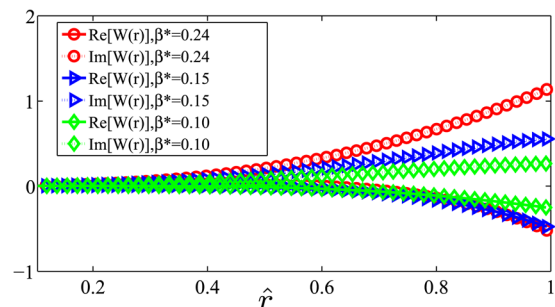


FIG. 8. (Color online) The radial distribution of the imaginary and the real parts of $W(r)$ in the RWM case, for various values of β^* , denoted by different colors.

increase of $\text{Im}(\delta W_{K0})$ with β^* in the RWM case. The magnitude of $\text{Re}[W(r)]$ also increases along the minor radius with fixed β^* . However, the radial profile of $\text{Re}[W(r)]$ is less sensitive to β^* . For example, the shape of the curve of $\text{Re}[W(r)]$ versus \hat{r} , for $\beta^* = 0.15$, is nearly the same as that for $\beta^* = 0.24$. At $\beta_{c,rwm}^* = 0.25$, the critical real frequency (in the plasma frame) of the RWM is $\Omega_{pf,c} = 0.8$ and the value of $\Omega_{d,e}/\Omega_{pf,c}$ is larger than unity over most of the profile from axis towards edge. For the RWM case, due to the lack of a transition from $\Omega_{d,e}/\Omega_{pf,c} > 1$ to $\Omega_{d,e}/\Omega_{pf,c} < 1$, the operator $\ln(1 - \Omega_{d,e}/\Omega_{pf,c})$ does not lead to the sharp change of $\text{Im}[W(r)]$ along the minor radius as EPs beta approaching $\beta_{c,rwm}^*$. That is the main reason that results in the difference of the $\text{Im}[W(r)]$ radial profile between the FLM and the RWM, shown in Figs. 6 and 8, respectively.

The imaginary part of δW_{K0} mainly comes from the resonance interaction between the mode real frequency and the EPs precession drift motion. Equation (15) shows that when the mode's real frequency and the EPs precession frequency satisfy the resonance condition $\omega_r - \omega_d - \omega_0 = 0$, the kinetic effect of EPs on the plasma instability becomes crucially important. A factor $\Re[=1/(\omega - \omega_d - \omega_0)]$ is introduced to represent the resonance operator. At the resonance position, the magnitude of $\text{Im}(\Re)$ increases as the mode growth rate decreases [i.e., $\text{Im}(\Re) = -1/\gamma$]. Even though the magnitude of $\text{Im}(\Re)$ approaches infinity as the mode growth rate vanishes, the radial integral of \Re stays finite. Figure 9 displays the magnitude of $\text{Im}(\Re)$ as functions of the EPs energy for different values of \hat{r} , for the RWM case with $\beta^* = 0.24$. At $\hat{r} = 1$, the RWM resonates with the trapped EPs with kinetic energy of about 67.5 KeV. However at $\hat{r} = 0.15$, the energy of the trapped EPs, required by the RWM-EPs resonance, is about 12 KeV. Figure 10 displays the real part of the operator \Re , as a function of the EPs kinetic energy at different minor radii. For a fixed value of \hat{r} , as the EPs kinetic energy goes through a special value, where the RWM-particle resonance occurs, the sign of $\text{Re}(\Re)$ changes from positive to negative. This leads to a cancellation of $\text{Re}(\Re)$ in the energy space integration through the resonance point. Consequently, the singularity due to the RWM-particle resonance does not significantly influence the value of $\text{Re}(\delta W_{K0})$. We point out, though, that the stabilization effect of trapped EPs on the RWM is indeed caused by the mode-particle resonance. Here, the occurrence of the resonance interaction is related to both the EPs' radial position

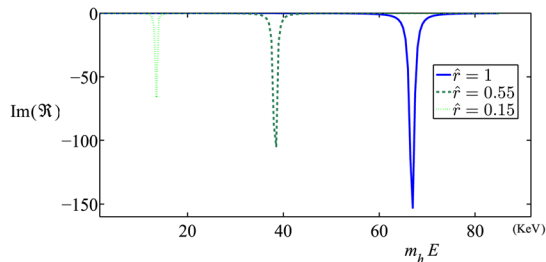


FIG. 9. (Color online) The imaginary part of the operator \Re versus the EPs kinetic energy, at various minor radii. The EPs beta is chosen as $\beta^* = 0.24$, at which the RWM's complex frequency (normalized to ω_{ds}) is $0.16 + 0.006i$.

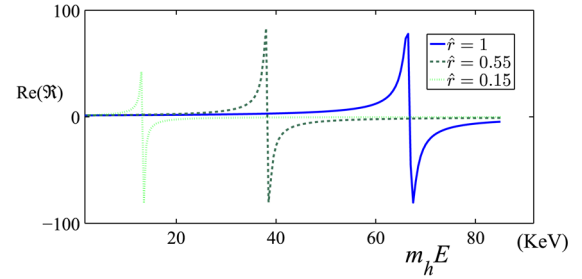


FIG. 10. (Color online) The real part of the operator \Re versus the EPs kinetic energy, at various minor radii. The EPs beta is chosen as $\beta^* = 0.24$.

and to their kinetic energy. For the FLM case, figures similar to Figs. 9 and 10 can also be obtained.

Figure 11 scans the mode-EPs resonance in a two-dimensional space: the EPs kinetic energy, $m_h E$, and the minor radius, \hat{r} . These are the two important parameters for the precession drift frequency of EPs while fixing the pitch angle. Along the curves, the resonance condition ($\Omega_r - \Omega_0 = \Omega_d$) is satisfied. In the RWM case (the dashed curve), the mode-particle resonance almost occurs along the whole minor radius. This mode-particle resonance interaction leads to the radial distribution of $\text{Im}[W(r)]$ keeping a finite value at all \hat{r} , as shown by the dotted-circle curves in Fig. 8. Here, the value of $\text{Im}[W(r)]$ is also related to the magnitude of the perpendicular displacement of the plasma in our theory model. On the other hand, for the FLM case (the solid curve), the mode-particle resonance only occurs in the radial region between \hat{r}_1 and \hat{r}_2 . In the region $\hat{r} > \hat{r}_2$, due to the lack of the mode-particle resonance, the amplitude of $\text{Im}[W(r)]$ is significantly smaller than that of $\text{Im}[W(r)]$ in the region $\hat{r}_1 < \hat{r} < \hat{r}_2$, as shown in Fig. 6. The resonance region becomes narrow as the FLM's real frequency increases. Figure 11 demonstrates why the magnitude of $\text{Im}(\delta W_{K0})$ for the FLM is much smaller than that for the RWM, as shown in Fig. 5(a). This significant reduction of $\text{Im}(\delta W_{K0})$ and the increase of $|\text{Re}(\delta W_{K0})|$ are responsible for triggering of the FLM.

B. Parametric study of the EPs effects

The influence of the plasma toroidal rotation speed on the RWM-EPs interaction has been studied in a previous paper.²² In this section, we mainly focus on the influence of the

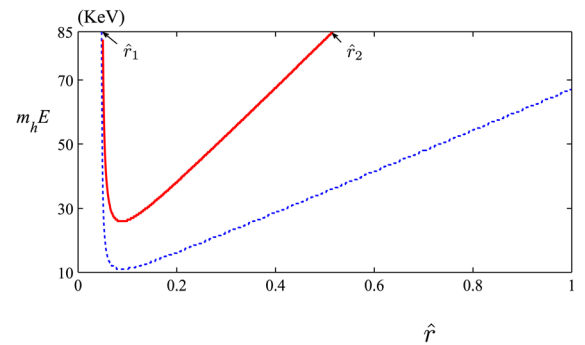


FIG. 11. (Color online) The resonant curves for the FLM (solid-red curve) and the RWM (dashed-blue curve) cases. The values of β^* for the FLM and the RWM are chosen as 0.166 and 0.24, respectively. The corresponding real frequencies, in the plasma frame for the FLM and the RWM, are 1.90 and 0.79, respectively.

plasma parameters on the behavior of the FLM instability. Figures 12(a) and 12(b) plot the growth rate and real frequency of the mode versus the EPs beta β^* , for the different values of Ω_0 . The calculations show that when $|\Omega_0| < 0.75$, the critical beta value β_c^* , for the onset of FLM, increases with decreasing the plasma rotation magnitude. A comparison between different curves (with different values of Ω_0) suggests that it is hard to excite the FLM with small values of $|\Omega_0|$. Figure 12(b) also shows that the initial real frequency of the FLM decreases with increasing the magnitude of $|\Omega_0|$. However, the slopes of the curves (the FLM growth rate and real frequency versus β^*) are nearly constant for different values of $|\Omega_0| (< 0.75)$.

At the rotation frequency of $\Omega_0 = -0.75$, the two branches (RWM and FLM) merge to each other, as shown by the dashed-blue curve in Fig. 12(a). This corresponds to a direct mode conversion (MC) between two instabilities. In other words, when the plasma rotation and the EPs beta are close to certain values, such that a resonance condition for the RWM-FLM resonance is satisfied, the MC between the RWM and the FLM leads to a general situation of avoided crossings in Fig. 3. For our case, the direct mode conversion occurs in an approximate region of $0.12 < \beta^* < 0.14$, where the mode possesses both the RWM character (growth rate decreasing with β^*) and the FLM character (real frequency increasing with β^*). At $\Omega_0 = -0.78$, the mode growth rate starts with that of the fluid RWM. After a weakly destabilization phase by the EPs kinetic effects, it then reaches a minimum value under the stabilizing effect from EPs. A further increase of the EPs beta finally causes a dramatic increase of the mode growth rate. The mode's real frequency is nearly a linear function of the EPs beta, similar to the case of $\Omega_0 = -0.75$. It can be expected that, at a sufficiently fast plasma rotation, the trapped EPs will provide predominantly

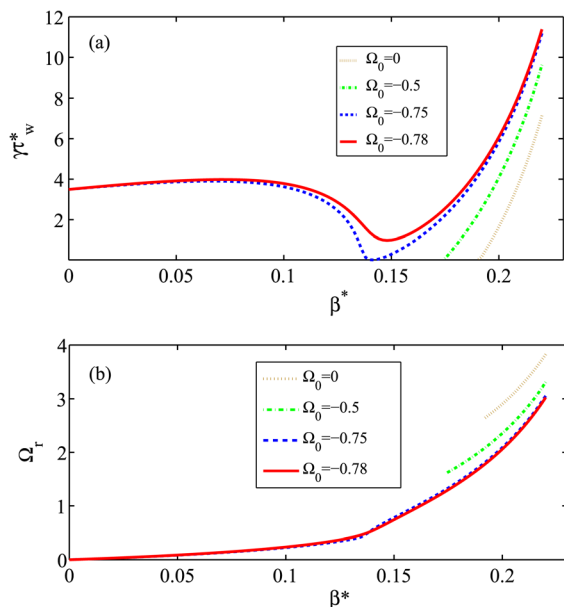


FIG. 12. (Color online) The normalized (a) mode's growth rates γ_w^* and (b) the corresponding mode real frequency Ω_r^* (in the wall frame), as functions of the EPs β^* . Different colors denote different choices of the plasma rotation frequency. The pitch angle is $\alpha_0 B_0 = 0.99$. The other parameters are the same as those presented in the beginning of Sec. III.

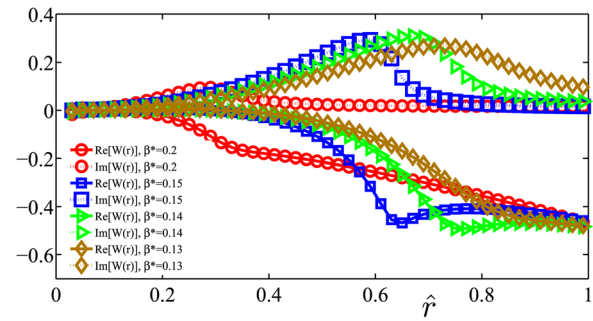


FIG. 13. (Color online) The radial profile of the imaginary and the real parts of $W(r)$ for the case with the RWM-FLM mode conversion, for various choices of the β^* values. The parameters $\alpha_0 B_0 = 0.99$ and $\Omega_0 = -0.78$ are assumed.

the destabilizing effect over the whole region of β^* . On the other hand, at relatively fast rotation, other potential damping mechanisms, such as that from continuum waves, or the kinetic damping from bounce motion of particles can become significant. Moreover, in the presence of MC, it should be hard to observe the periodic bursting behavior of the FLM, as well as the coexistence of the FLM and the RWM in experiments.

Shown in Fig. 13 are the radial distributions of $\text{Re}[W(r)]$ and $\text{Im}[W(r)]$ for various values of β^* for the case with the RWM-FLM MC. The normalized mode complex frequency, at $\beta^* = 0.2, 0.15, 0.14$, and 0.13 , are $2.06 + 0.41i$, $0.74 + 0.07i$, $0.54 + 0.09i$, and $0.41 + 0.16i$, respectively. At large $\beta^* (= 0.2)$, the radial distribution of $W(r)$ is similar to that of the FLM case shown in Fig. 6. On the other hand, as the EPs β^* decreases ($\beta^* = 0.13$), the radial profile of $W(r)$ approaches to that of the RWM shown in Fig. 8. It is worthwhile to notice that, with β^* varying from large to small values, the radial profile of $W(r)$ smoothly changes from the red-circle curve to the brown-diamond curve, with no appearance of singular points along the minor radius.

Since the wall time in ITER is about two orders of magnitude larger than that of the present day tokamak devices, such as DIII-D and JT-60U, it is useful, for the ITER prediction, to study the dependence of the FLM instability on the wall penetration time. Figure 14 presents (a) the growth rate and (b) the real frequency of the mode versus β^* , for various choices of the wall time τ_w^* . At a short wall time $\tau_w^* = 0.7\tau_{w0}^*$ ($\tau_{w0}^* = 2\text{ms}$), the MC can occur. Moreover, the critical value β_c^* for the onset of FLM becomes larger with increasing τ_w^* . This is because a wall with larger τ_w^* can provide more stabilization on the external instability than a wall with smaller τ_w^* . Although the initial real frequency of the FLM depends on the wall time, the magnitude of Ω_r barely changes, while varying the wall time τ_w^* at relatively large $\beta^* (> 0.21)$. In other words, when the EPs beta is sufficiently large, the mode's real frequency is nearly independent of the wall time.

The effect of the EPs pitch angle on the characteristics of the FLM is shown in Fig. 15. A comparison of the cases with $\alpha_0 B_0 = 1.18$ and $\alpha_0 B_0 = 0.99$ shows that the latter leads to only one unstable FLM branch, with an initial real frequency (in the plasma frame) $\Omega_{pf,c} (> 1)$, as shown by the dashed curves in Figs. 3 and 4. However, for the case with

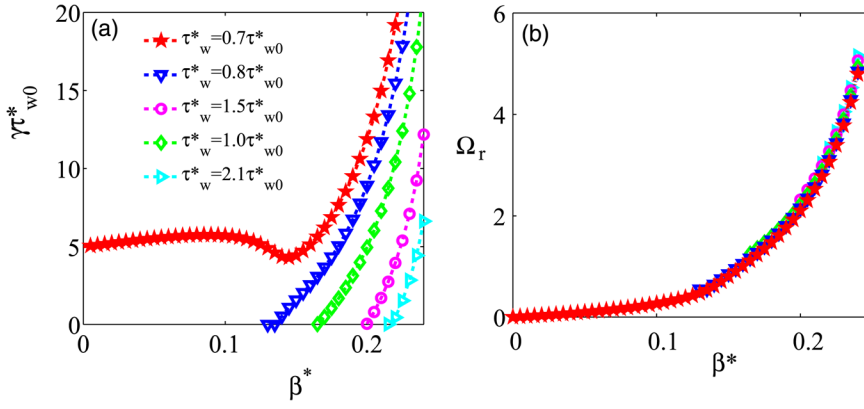


FIG. 14. (Color online) The (a) mode's growth rate and (b) real frequency (in the wall frame) as functions of β^* , for various choices of the wall time τ_w^* . Here, $\tau_{w0}^* = 2$ ms is the typical field penetration time with the wall conductivity $\sigma = 10^6 \Omega^{-1} \text{m}^{-1}$.

$\alpha_0 B_0 = 1.18$, besides the FLM branch with a relatively large $\Omega_{pf,c} (> 1)$, there is another unstable FLM branch (named the second FLM branch), with an initial real frequency $\Omega_{pf,c}$ almost equal to 1. The growth rate of the second FLM branch first increases with the EPs beta, then decreases to almost zero at $\beta^* = 0.1$. It is interesting to notice that the curves with $\alpha_0 B_0 = 1.18$ and $\alpha_0 B_0 = 1.207$ indicate that there can be many critical points for the dispersion relation Eq. (11), at certain values of the pitch angle. In fact, there is a narrow stable window for the FLM in the β^* space, for the cases with $\alpha_0 B_0 = 1.18$ and 1.207. The characteristic of this narrow stable window is similar to the second stable region of the classical fishbone mode.³⁶ The critical value for the onset of the second FLM branch, for $\alpha_0 B_0 = 1.18$, is about 0.04, much smaller than that needed for the FLM branch with $\Omega_{pf,c} > 1$. With increasing the pitch angle ($\alpha_0 B_0 = 1.21$), the two FLM branches merge into one instability, with the initial real frequency $\Omega_{pf,c} (= 1)$. At $\alpha_0 B_0 = 1.25$, the critical value of β_c^* is 0.04, which is significant smaller than that at $\alpha_0 B_0 = 0.99$. In fact, there seems exist a critical value of the pitch angle, beyond which the critical β_c^* , for triggering FLM, jumps from one large value to a small value.

Since the pitch angle of EPs is often determined by the injection angle of neutral beams, multiple critical points may be observed in experiments, by scanning the EPs beta for appropriate injection angles of neutral beams. It seems that the case of an FLM with the initial real frequency $\Omega_{pf,c} (= 1)$ is closer to the observations in the present tokamak devices.²⁷

Figure 16 illustrates the dependence of the precession frequency of trapped EPs on the minor radius, for different choices of the pitch angle. For comparison, the case with $\alpha_0 B_0 = 0.99$ is also plotted. At $\alpha_0 B_0 = 1.1$, the normalized precession frequency decreases along the minor radius. For this pitch angle,

the EPs in the core region of the plasma are passing particles only. Figure 16 shows that the existence region of trapped EPs, along the minor radius, significantly depends on the EPs pitch angle. In other words, when the EPs distribution function is assumed to be the delta-function of the pitch angle, the region of trapped EPs becomes narrower in the minor radius, as the value of pitch angle is above 1 and increases.

IV. EFFECTS OF EPS ON THE $m/n = 3/1$ MODES

In order to understand how the variation of the mode eigenfunction affects our drift kinetic analysis, additional investigation is carried out in this section, for the $m/n = 3/1$ mode. The EPs kinetic contribution to the RWM dispersion relation, δW_{K0} [similar to Eq. (16)], can also be obtained for the 3/1 mode

$$\delta W_{K0} = \int_{\hat{r}_{\min}}^1 W(r) d\hat{r}, \quad (18)$$

where

$$W(r) = \frac{8\pi\beta_h}{Aa} \left(1 - \frac{\alpha_0 B_0}{2}\right)^2 R a^{2m-2} \hat{r}^{2(m-1)} \hat{r}^{-1/2} Y_1, \quad (19)$$

$$Y_1 = \left\{ \Omega_{pf} [\hat{A}_1 - \hat{B}_1 - 2\hat{C}_1 K_b / (K_2 q) + \hat{D}_1 K_b / (K_2 q)] - \Omega_{pf}^2 [\hat{B}_1 + \hat{C}_1 K_b / (K_2 q)] \frac{\partial}{\partial \Omega_{pf}} \right\} H + (\hat{D}_1 - \hat{C}_1) K_b / (K_2 q), \quad (20)$$

$$H = \frac{1}{\Omega_{d,e}} \ln(1 - \Omega_{d,e} / \Omega_{pf}). \quad (21)$$

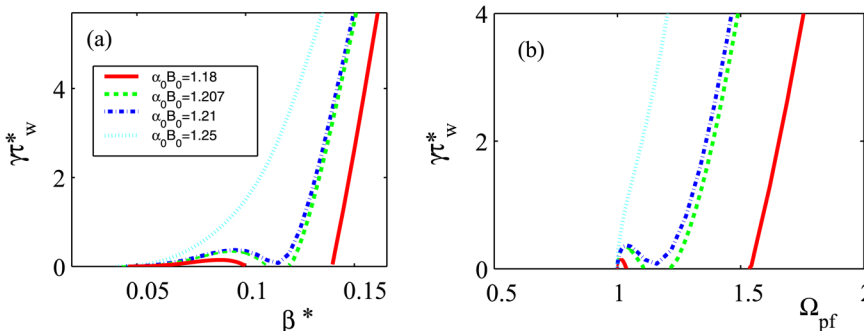


FIG. 15. (Color online) The FLM growth rate versus (a) EPs beta β^* and (b) the real frequency (in the plasma frame) of the mode, for various choices of the trapped EPs pitch angle. The plasma rotation frequency is assumed as $\Omega_0 = -0.63$.

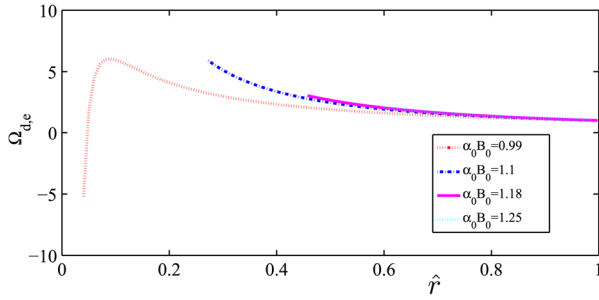


FIG. 16. (Color online) The radial profile of the normalized precession frequency of trapped EPs, for various values of the pitch angle $\alpha_0 B_0$.

The expressions for the coefficients \hat{A}_1 , \hat{B}_1 , \hat{C}_1 , and \hat{D}_1 are presented in the Appendix.

Figure 17 displays (a) the normalized mode's growth rate and (b) the real mode frequency, for the $m/n = 3/1$ mode. The bursting fishbone like instability, with the $m/n = 3/1$ eigenstructure, still occurs when β^* exceeds a threshold value. This confirms that the appearance of the FLM is not sensitive to the mode number. We mention that the experimental observation in JT-60U has shown EPs-driven bursting modes possessing the $3/1$ structure at the plasma edge. Moreover, the $m/n = 2/1$ and $m/n = 3/1$ FLMs can couple to each other in a torus. This coupling of FLMs with different mode numbers may provide a partial interpretation of the bursting mode distortion, observed in the recent DIII-D experiments.^{26,37}

V. SUMMARY AND DISCUSSIONS

Kinetic effects of trapped EPs on the external kink modes, in the presence of a resistive wall, are investigated, using the kinetic RWM dispersion relation. Our results show that, at $\alpha_0 B_0 = 0.99$ in our study, when the perpendicular beta β^* of trapped EPs exceeds a critical value β_c^* , the FLM instability with an external kink eigenstructure is triggered, which rapidly grows with increasing β^* ($> \beta_c^*$) and eventually becomes a dominant instability. The real frequency of the FLM matches the range of the magnetic precession frequency of trapped EPs. These characteristics of the FLM are qualitatively consistent with the experimental observations in both JT-60U and DIII-D devices.^{25,27}

The radial profile, $\text{Im}[W(r)]$, of the imaginary part of the EPs drift kinetic energy, in the FLM case, is rather different

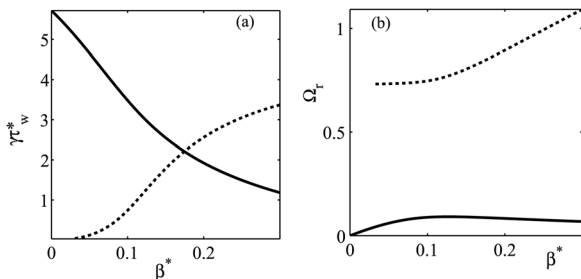


FIG. 17. The (a) growth rate and (b) real frequency of the $m/n = 3/1$ FLM (dashed curve) and the RWM (solid curve) instabilities as functions of β^* . The other parameters are chosen as $B_0 = 2.3T$, $q = 2.3$, $\delta\hat{W}_r^\infty = -0.17$, $\delta\hat{W}_b^\infty = 0.029$, $\alpha_0 B_0 = 0.99$, $\tau_{*w} = 2$ ms, and $\Omega_0 = -0.6$.

from that in the RWM case. In the FLM case, due to the disappearance of the mode-particle resonance in the larger \hat{r} region, the radial distribution of $\text{Im}[W(r)]$ has a sharp reduction at a certain radial position. In the RWM case, on the other hand, the $\text{Im}[W(r)]$ has a radial distribution with finite values from the core through the edge, without singular points along the minor radius. The significant reduction of $\text{Im}(\delta W_{K0})$, induced by the special $\text{Im}[W(r)]$ radial profile, and increase of $|\text{Re}(\delta W_{K0})|$ are responsible for triggering the FLM.

We also find that a mode conversion between the RWM and the FLM can directly occur. In the conversion region, the mode possesses the characteristics of both RWM (growth rate decreasing with β^*) and FLM (real frequency increasing with β^*). For the case with mode conversion, the radial profile of $W(r)$ is similar to that of the FLM at large values of β^* . At relatively small values of β^* , it is similar to that of the RWM case.

The critical value β_c^* , for the onset of the FLM, increases with decreasing the magnitude of the plasma rotation frequency. The value of β_c^* becomes larger when the wall time becomes longer. However, the real frequency of the FLM is less sensitive to the above two quantities (the plasma rotation and the wall time). The growth rate of the FLM is rather sensitive to the pitch angle of trapped EPs. At certain pitch angles, e.g., $\alpha_0 B_0 = 0.99$ in our study, there are multiple critical points for the dispersion relation Eq. (11). At sufficiently large pitch angle, such as $\alpha_0 B_0 = 1.21$, the FLM instability occurs, with the normalized initial frequency exactly equal to unity. We find that there can be a critical pitch angle, beyond which the critical β_c^* , for triggering the FLM, jumps from one large value to a small value. We also find the FLM instability with an $m/n = 3/1$ external eigenmode structure, indicating that the occurrence of the FLM is not sensitive to the mode number.

Finally, we point out that our theory model can be extended to include the spatial distribution of EPs, for a more realistic investigation of the off-axis neutral beam injection heated plasmas.

ACKNOWLEDGMENTS

This work was supported by the National Natural Science Foundation of China under Grant No. 10775040 and also supported in part by National Magnetic Confinement Fusion Science Program under Grant No. 2009 GB101002.

APPENDIX: EXPRESSIONS FOR \hat{A}_1 , \hat{B}_1 , \hat{C}_1 , AND \hat{D}_1

Here, we list the expressions for the coefficients \hat{A}_1 , \hat{B}_1 , \hat{C}_1 , and \hat{D}_1 , appearing in Eq. (20), derived for the $m/n=3/1$ mode eigenfunction

$$\hat{A}_1 = \left(-\frac{1}{9} \frac{K}{2\alpha_0 B_0} \Lambda_1 - \frac{1}{2\alpha_0 B_0} \Lambda \frac{dK}{dk_t} \right), \quad (\text{A1})$$

$$\hat{B}_1 = \left\{ -\frac{1}{\alpha_0 B_0} \frac{K_b}{K_2} \Lambda K \frac{d}{dk_t} \left(\frac{E}{K} \right) \right\}, \quad (\text{A2})$$

$$\hat{C}_1 = \frac{K\Lambda}{2E-K} \left[(1-2k_t)K \frac{d}{dk_t} \left(\frac{E}{K} \right) - (2E-K) \right], \quad (\text{A3})$$

$$\hat{D}_1 = \left[\left(\frac{1}{9} K \frac{1-2k_t}{2} \Lambda_1 - \frac{1}{2} \Lambda K + \Lambda \frac{1}{2} (1-2k_t) \frac{dK}{dk_t} \right) + \Lambda K (2m-2) \right], \quad (\text{A4})$$

$$\Lambda = \frac{1}{9} \left[\begin{aligned} &64 \frac{E^2}{K^2} (4k_t^2 - 4k_t + 1) + 16 \frac{E}{K} (-16k_t^2 + 18k_t - 5) \\ &+ 64k_t^2 - 80k_t + 25 \end{aligned} \right], \quad (\text{A5})$$

$$\Lambda_1 = \left\{ \begin{aligned} &\left[128(4k_t^2 - 4k_t + 1) \frac{E}{K} + 16(-16k_t^2 + 18k_t - 5) \right] \frac{d}{dk_t} \left(\frac{E}{K} \right) \\ &+ \left[64 \frac{E^2}{K^2} (8k_t - 4) + \frac{E}{K} 16(-32k_t + 18) + 128k_t - 80 \right] \end{aligned} \right\}. \quad (\text{A6})$$

- ¹A. Bondeson and D. J. Ward, *Phys. Rev. Lett.* **72**, 2709 (1994).
²R. Betti and J. P. Freidberg, *Phys. Rev. Lett.* **74**, 2949 (1995).
³M. S. Chu, J. M. Greene, T. H. Jensen, R. L. Miller, A. Bondeson, R. W. Johnson, and M. E. Mauel, *Phys. Plasmas* **2**, 2236 (1995).
⁴D. Gregoratto, A. Bondeson, M. S. Chu, and A. M. Garofalo, *Plasma Phys. Controlled Fusion* **43**, 1425 (2001).
⁵L. J. Zheng, M. Kotschenreuther, and M. S. Chu, *Phys. Rev. Lett.* **95**, 255003 (2005).
⁶D. J. Ward and A. Bondeson, *Phys. Plasmas* **2**, 1570 (1995).
⁷A. Bondeson and M. S. Chu, *Phys. Plasmas* **3**, 3013 (1996).
⁸A. B. Mikhailovskii and G. I. Suramlshvili, *Fiz. Plasmy* **6**, 933 (1979) [*Sov. J. Plasma Phys.* **5**, 523 (1979)].
⁹A. B. Mikhailovskii and V. S. Tsypin, *Fiz. Plasmy* **9**, 147 (1983) [*Sov. J. Plasma Phys.* **9**, 91 (1983)].
¹⁰A. B. Mikhailovskii and B. N. Kuvshinov, *Plasma Phys. Rep.* **21**, 802 (1995) [*Fiz. Plasmy* **21**, 849 (1995)].
¹¹C. G. Gimblett and R. J. Hastie, *Phys. Plasmas* **7**, 258 (2000).
¹²G. Z. Hao, Y. Q. Liu, and A. K. Wang, in *Proceedings of the 23rd International Conference on Fusion Energy, Daejeon, Korea, 2010*, (IAEA, Vienna), Paper No. THS/P5. and http://www-pub.iaea.org/mtcd/meetings/PDFplus/2010/cn180/cn180_papers/th_s_p5-07.pdf.
¹³H. Reimerdes, A. M. Garofalo, G. L. Jackson, M. Okabayashi, E. J. Strait, M. S. Chu, Y. In, R. J. La Haye, M. J. Lanctot, Y. Q. Liu, G. A. Navratil, W. M. Solomon, H. Takahashi, and R. J. Groebner, *Phys. Rev. Lett.* **98**, 055001 (2007).
¹⁴M. Takechi, G. Matsunaga, N. Aiba, T. Fujita, T. Ozeki, Y. Koide, Y. Sakamoto, G. Kurita, A. Isayama, Y. Kamada, and the JT-60 team, *Phys. Rev. Lett.* **98**, 055002 (2007).
¹⁵G. Z. Hao, A. K. Wang, Y. Q. Liu, and X. M. Qiu, *Phys. Rev. Lett.* **107**, 015001 (2011).
¹⁶Y. Liu, M. S. Chu, I. T. Chapman, and T. C. Hender, *Nucl. Fusion* **49**, 035004 (2009).
¹⁷Y. Q. Liu, M. S. Chu, C. G. Gimblett, and R. J. Hastie, *Phys. Plasmas* **15**, 092505 (2008).
¹⁸Y. Q. Liu, M. S. Chu, I. T. Chapman, and T. C. Hender, *Phys. Plasmas* **15**, 112503 (2008).
¹⁹B. Hu and R. Betti, *Phys. Rev. Lett.* **93**, 105002 (2004).
²⁰B. Hu, R. Betti, and J. Manickam, *Phys. Plasmas* **12**, 057301 (2005).
²¹H. Reimerdes, J. W. Berkery, M. J. Lanctot, A. M. Garofalo, J. M. Hanson, Y. In, M. Okabayashi, S. A. Sabbagh, and E. J. Strait, *Phys. Rev. Lett.* **106**, 215002 (2011).
²²G. Z. Hao, Y. Q. Liu, A. K. Wang, H. B. Jiang, G. Lu, H. D. He, and X. M. Qiu, *Phys. Plasmas* **18**, 032513 (2011).
²³G. Matsunaga, K. Shinohara, N. Aiba, Y. Sakamoto, A. Isayama, N. Asakura, T. Suzuki, M. Takechi, N. Oyama, H. Urano, and the JT-60 Team, *Nucl. Fusion* **50**, 084003 (2010).
²⁴Y. Q. Liu, *Nucl. Fusion* **50**, 095008 (2010).
²⁵M. Okabayashi, I. N. Bogatu, M. S. Chance, M. S. Chu, A. M. Garofalo, Y. In, G. L. Jackson, and R. J. La Haye, *Nucl. Fusion* **49**, 125003 (2009).
²⁶M. Okabayashi, G. Matsunaga, J. S. deGrassie, W. W. Heidbrink, Y. In, Y. Q. Liu, H. Reimerdes, W. M. Solomon, E. J. Strait, M. Takechi, N. Asakura, R. V. Budny, G. L. Jackson, J. M. Hanson, R. J. La Haye, M. J. Lanctot, J. Manickam, K. Shinohara, and Y. B. Zhu, *Phys. Plasmas* **18**, 056112 (2011).
²⁷G. Matsunaga, N. Aiba, K. Shinohara, Y. Sakamoto, A. Isayama, M. Takechi, T. Suzuki, N. Oyama, N. Asakura, Y. Kamada, T. Ozeki, and JT-60 Team, *Phys. Rev. Lett.* **103**, 045001 (2009).
²⁸M. S. Chu and M. Okabayashi, *Plasma Phys. Controlled Fusion* **52**, 123001 (2010).
²⁹P. J. Catto, W. M. Tang, and D. E. Baldwin, *Plasma Phys.* **23**, 639 (1981).
³⁰L. Chen, R. B. White, and M. N. Rosenbluth, *Phys. Rev. Lett.* **52**, 1122 (1984).
³¹T. M. Antonsen and B. Lane, *Phys. Fluids* **23**, 1205 (1980).
³²S. W. Haney and J. P. Freidberg, *Phys. Fluids B* **1**, 1637 (1989).
³³J. W. Berkery, S. A. Sabbagh, H. Reimerdes, R. Betti, B. Hu, R. E. Bell, S. P. Gerhardt, J. Manickam, and M. Podesta, *Phys. Plasmas* **17**, 082504 (2010).
³⁴R. B. White, L. Chen, F. Romanelli, and R. Hay, *Phys. Fluids* **28**(1), 278 (1985).
³⁵Y. Wu, C. Z. Cheng, and R. B. White, *Phys. Plasmas* **1**, 3369 (1994).
³⁶H. D. He, J. Q. Dong, G. Y. Fu, Z. X. He, H. B. Jiang, Z. T. Wang, G. Y. Zheng, F. Liu, Y. X. Long, Y. Shen, and L. F. Wang, *Nucl. Fusion* **51**, 113012 (2011).
³⁷W. W. Heidbrink, M. E. Austin, R. K. Fisher, M. Garcia-Munoz, G. Matsunaga, G. R. McKee, R. A. Moyer, C. M. Muscatello, M. Okabayashi, D. C. Pace, K. Shinohara, W. M. Solomon, E. J. Strait, M. A. Van Zeeland, and Y. B. Zhu, *Plasma Phys. Controlled Fusion* **53**, 085028 (2011).